Automatic 3D image registration for nano-resolution chemical mapping using synchrotron spectro-tomography

Jin Zhang,[a,b,c] Jun Hu,[d] Zhisen Jiang,[b] Kai Zhang,[a] Peng Liu,[a] Chaonan Wang,[e] Qingxi Yuan,[a]* Piero Pianetta[b] and Yijin Liu[b]*

[a]Beijing Synchrotron Radiation Facility, Institute of High Energy Physics, Chinese Academy of Sciences, Beijing 100049, People's Republic of China, [b]Stanford Synchrotron Radiation Lightsource, SLAC National Accelerator Laboratory, Menlo Park, CA 94025, USA, [c]University of Chinese Academy of Sciences, Beijing 100049, People's Republic of China, [d]School of Materials Science and Engineering, Nanjing Institute of Technology, Nanjing, Jiangsu 211167, People's Republic of China, and [e]School of Science, Nantong University, Nantong, Jiangsu 226019, People's Republic of China. *Correspondence e-mail: yuanqx@ihep.ac.cn, liuyijin@slac.stanford.edu

Nano-resolution synchrotron X-ray spectro-tomography has been demonstrated as a powerful tool for probing the three-dimensional (3D) structural and chemical heterogeneity of a sample. By reconstructing a number of tomographic data sets recorded at different X-ray energy levels, the energy-dependent intensity variation in every given voxel fingerprints the corresponding local chemistry. The resolution and accuracy of this method, however, could be jeopardized by non-ideal experimental conditions, *e.g.* instability in the hardware system and/or in the sample itself. Herein is presented one such case, in which unanticipated sample deformation severely degrades the data quality. To address this issue, an automatic 3D image registration method is implemented to evaluate and correct this effect. The method allows the redox heterogeneity in partially delithiated $Li_xTa_{0.3}Mn_{0.4}O_2$ battery cathode particles to be revealed with significantly improved fidelity.

1. Introduction

Tomography is a groundbreaking development in the field of X-ray imaging, and was highlighted by the Nobel Prize in Physiology or Medicine in 1979 (https://www.nobelprize.org/prizes/medicine/1979/summary/). Tomography non-invasively reconstructs the 3D internal structure of a sample from a number of projection images collected at different viewing angles. The tremendous success of X-ray tomography is evident by its broad contributions to research (Buffiere *et al.*, 2010), industry (De Chiffre *et al.*, 2014) and medicine (Brenner & Hall, 2007). When implemented at synchrotron facilities, tomography can be executed in different modalities (Sakdinawat & Atwood, 2010) at much faster speed (Yang *et al.*, 2020) and higher spatial resolution (Dierolf *et al.*, 2010). The synchrotron's advantages in spatial coherence (Eastwood *et al.*, 2015; Zhu *et al.*, 2010), monochromaticity (Torikoshi *et al.*, 2003) and, subsequently, compositional and chemical sensitivities (Kao *et al.*, 2013; Liu, Meirer, Wang *et al.*, 2012; Wei *et al.*, 2018) collectively open vast scientific opportunities. One of the most popular approaches is to combine X-ray tomography with X-ray absorption spectroscopy (Yang *et al.*, 2014, 2019; Yu, Farmand *et al.*, 2018; Hitchcock, 2015; Masci *et al.*, 2019; Nelson *et al.*, 2011; Zhang *et al.*, 2020; Zhu *et al.*, 2020; Wang *et al.*, 2016), featuring a much desired experimental capability that could spatially resolve chemical heterogeneity by probing

| Overlay of two images | Edge detection | Contour registration |
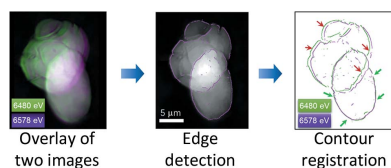
spatially resolved X-ray spectroscopic signals. This is because the structural and chemical heterogeneities are not only ubiquitous in real-world functional materials but also are often interdependent, complicating the material system while also providing an opportunity for advanced functional materials engineering.

As a specific example, we discuss here the study of battery cathode particles using nano-resolution spectro-tomography (Wei *et al.*, 2018). This is a very active research field. Both soft and hard X-rays have been utilized to investigate the redox heterogeneity in a battery cathode, which is modulated by the local electrochemistry (Yang *et al.*, 2019). While soft X-rays have demonstrated excellent sensitivity to the chemical states of the battery cathode via accessing the absorption L edges of the transition metal elements (Yu, Farmand *et al.*, 2018), their limited penetration depth has set some practical constraints on the experiment. Hard X-rays, on the other hand, are more robust to various experimental implementations, although spectroscopy in the hard X-ray regime often requires the energy to be scanned in relatively fine steps across the absorption K edges of the transition metal elements.

In this work, we focus on hard X-ray full-field spectro-tomography using nano-resolution transmission X-ray microscopy (TXM) for X-ray absorption near-edge structure (XANES) imaging (Meirer *et al.*, 2011; Nelson *et al.*, 2011). While the pre-edge and the post-edge regions can be scanned with large energy steps, the near-edge region requires fairly good energy resolution for the desired sensitivity to different chemical species. Therefore, in a typical experiment of this kind, 3D tomograms are collected at several tens of energy levels, which not only is very time-consuming (a typical 3D XANES scan takes over 10 h on beamline 6-2c at the Stanford Synchrotron Radiation Lightsource) but also generates a large amount of data. These raw images need to be processed through a number of data reduction and reconstruction steps before they are converted into a useful form for further scientific interpretation. Although standard data-reduction pipelines and algorithms have been developed (Liu, Meirer, Williams *et al.*, 2012; Yang *et al.*, 2015), they rely on assumptions of rigidity and stability of the sample. Unanticipated sample motion and deformation can happen in practice and could jeopardize the data quality severely.

Herein, we present one such case, in which the sample deformed slightly during the measurement. In this case, the conventional registration approach (Yu, Xia *et al.*, 2018) based on the alignment of projection images failed. We present our implementation of a 3D registration method to compensate for the unanticipated sample motion/deformation after the tomograms are reconstructed. While rigid sample motion is a common problem that has been broadly studied, sample deformation could impact the results more severely and is a key issue that we are trying to address in our approach. Our result demonstrates considerable advantages over the conventional approach and enables us to reveal the chemical complexity in the studied $Li_xTa_{0.3}Mn_{0.4}O_2$ battery cathode particles with significantly improved fidelity.

2. Experimental methods

2.1. Sample preparation

The $Li_xTa_{0.3}Mn_{0.4}O_2$ (LTMO) sample was prepared by chemical delithiation, which reacted a pristine $Li_{1.3}Ta_{0.3}Mn_{0.4}O_2$ crystal with $0.1\,M$ nitronium tetrafluoro-borate (NO_2BF_4) in acetonitrile solution in an argon-filled glove box ($O_2 < 1$ p.p.m. and $H_2O < 1$ p.p.m.) for 1–4 days. The sample was then washed with acetonitrile several times and dried overnight. For more details, we refer to the published literature (Kan *et al.*, 2019).

2.2. Nano-resolution X-ray spectro-tomography

X-ray spectro-tomography using transmission X-ray microscopy (TXM) was performed on beamline 6-2c at the Stanford Synchrotron Radiation Lightsource (SSRL). More details about the TXM setup can be found elsewhere (Andrews *et al.*, 2011). The LTMO particles were loaded into a quartz capillary, which was rotated from $-90°$ to $90°$ with an angular step size of $1°$. As well as angle rotation, 3D spectro-tomography also does an energy scan across the K edge of Mn. The steps of the energy scan were 15 eV in the region away from the near-edge region and 3 eV in the near-edge region.

3. Results and discussion

We present our approach for handling the 3D imaging results on $Li_xTa_{0.3}Mn_{0.4}O_2$ battery cathode particles that tilted slightly during the acquisition of the spectro-tomographic data (Kan *et al.*, 2019). We focused on the Mn K edge because the redox activity of the Mn cation in this material is one of the major charge-compensation mechanisms for the cathode during battery operation. Therefore, imaging the spatial distribution of the Mn valence state over the cathode particles could offer valuable insights into reaction heterogeneity and performance degradation, which formulate our scientific motivation.

In a typical X-ray spectro-microscopic experiment using a transmission X-ray microscopy (TXM), a series of projection images are acquired as the energy of the incident X-ray is scanned across the Mn K edge [see schematic illustration in Fig. 1(*a*)]. This standard experimental procedure has been well established and is often referred to as 2D XANES imaging. After a few image-processing steps, including flat-field and dark-field corrections, magnification correction and image alignment, a certain pixel's intensity variation as a function of the incident X-ray energy can be extracted, representing the corresponding local XANES spectrum. In the present case, however, we observed severely distorted XANES spectra over the regions near the edge of the particle [see Fig. 1(*b*)]. For troubleshooting, we take a closer look at the data by overlapping two projection images collected at two different energy levels [Fig. 1(*c*)]. A direct comparison of this image pair suggests that the images are not well registered [left panel in Fig. 1(*c*)]. For a more accurate analysis, we utilized the *Canny* edge-detection algorithm (Green, 2002) to better define the particle boundary [middle panel in Fig. 1(*c*)]. The overlapped view [right panel in Fig. 1(*c*)] clearly suggests that
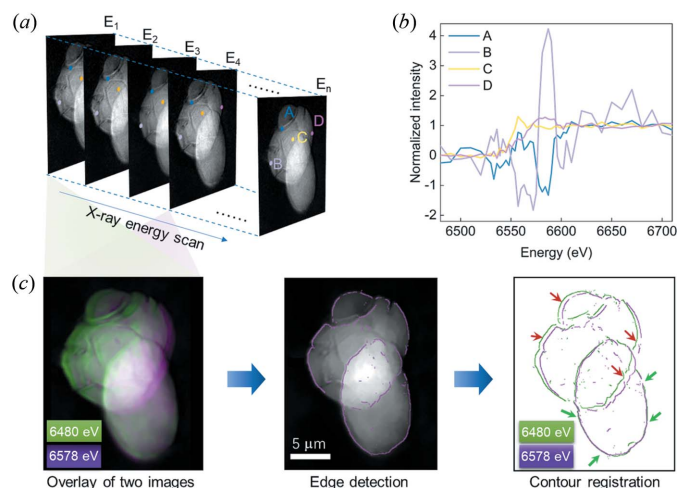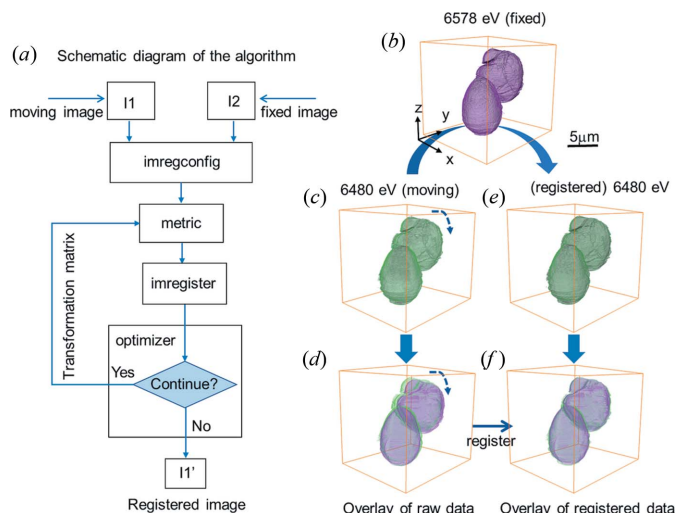
Figure 1
(a) Illustrating a series of 2D transmission projection images of $Li_xTa_{0.3}Mn_{0.4}O_2$ cathode particles with the incident X-ray energy scanned across the Mn K edge. (b) A normalized intensity plot of the selected pixels in panel (a). (c) An overlay of two projection images and the detected contours of the particles. The green arrows in the right-hand panel show good alignment for the lower particle, while the red arrows show the misalignment for the upper particle.

Figure 2
(a) A schematic diagram of the 3D registration algorithm. Panels (b) and (c) are 3D renderings of the tomogram collected at 6578 eV (fixed data) and 6480 eV (moving data), respectively. The aligned tomogram at 6480 eV is shown in panel (e). Panels (d) and (f) are the overlays of the raw image pair and the aligned image pair, respectively.

these two particles have moved relative to each other. While the lower particle is nicely aligned (as indicated by the green arrows), the higher particle is clearly tilted (red arrows). Therefore, the conventional image-registration procedure based on 2D alignment algorithms has failed in this case.

We highlight again that spectro-tomography is a rather time-consuming technique. Several tens of tomographic scans are executed at different X-ray energy levels across the absorption edge. It is at least an overnight scan on beamline 6-2c at the SSRL. The conventional data-reduction pipeline relies on assumptions of rigidity and stability of the sample, which are clearly not satisfied in the present case. Advanced 3D registration with robustness to sample deformation is needed for correcting the particle motion in our data. By analyzing projection images in a given view angle at different energies, we conclude that the motion of the top particle is rather slow, which indicates that the motion-induced artifacts in each individual tomogram are at a relatively low level. Therefore, we reconstructed the tomograms at all the different energy levels separately, prior to 3D registration.

With the reconstructed tomograms as input, our desired functionality is to register these 3D data sets in a way that is automatic and robust to the sample's nonrigidity. In this work, as illustrated schematically in Fig. 2(a), we utilized an intensity-based image-registration function, imregister, that is available in MATLAB's image-processing toolbox (details shown in the supporting information). While more details can be found in the MATLAB documentation, we briefly describe the working principle here. The employed imregister function is an iterative process that takes a pair of 3D images (a moving image and a fixed image) as input and registers the moving image to the fixed one. We chose the mean-squared error (MSE) between the two images as an indicator of the

degree of alignment between the two images. The goal of this iterative process is to formulate a geometric transformation for the moving tomogram to minimize the cost function, which is set to be the MSE between the fixed tomogram and the transformed moving tomogram in our case. Considering the deformation, and thus the nonrigidity, of our sample, we chose the 'affine' geometric transformations, which include translation, rotation, scale and shear operations. All of these settings are specified using the function imregconfig. Specific to our implementation, we chose to use the 3D tomogram at the highest energy (6710 eV) as the fixed image. The other tomograms (the moving images) are registered to the fixed image sequentially. It is important to point out that the absorption coefficient, i.e. the absolute intensity in the reconstructed tomogram, is intrinsically different at different X-ray energies, which can lead to different residual values in the MSE. To rule out this effect, we binarized the raw tomograms by conducting an automatic segmentation procedure based on their respective intensity histograms, before feeding them into the registration engine. For visualization we show, in Fig. 2(f) as an example, the registration procedure and the comparison of the results for a selected tomogram pair.

To evaluate the accuracy of our 3D registration operation, we carried out a systematic comparison of the raw and aligned tomograms across all the scanned energy levels. By evaluating the MSE between two different tomograms, the quality of the 3D registration can be quantified. The 3D rendering of the squared difference of the original data set is shown in Fig. 3(a), which clearly indicates that the bottom particle is fairly well aligned while the top particle shows noticeable movement. As shown in Fig. 3(b), the difference is reduced after the 3D registration procedure. The suppression of the misalignment-induced 3D image difference is unambiguous. The MSE is further calculated for all the tomograms across the scan
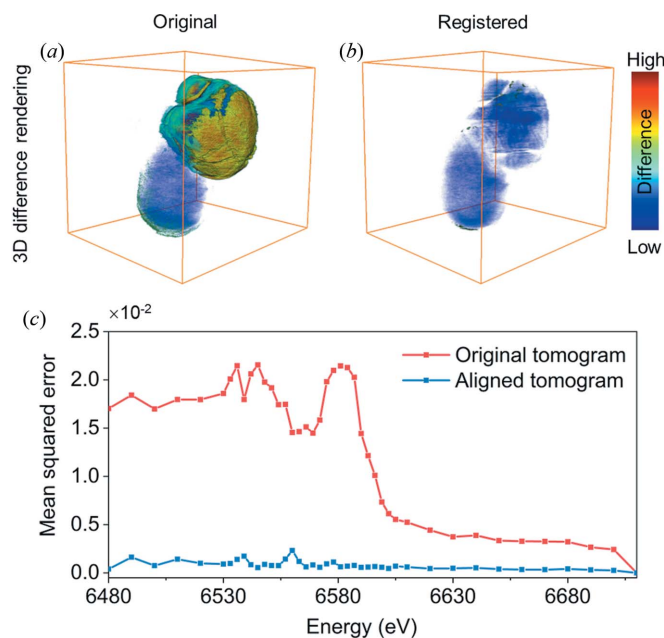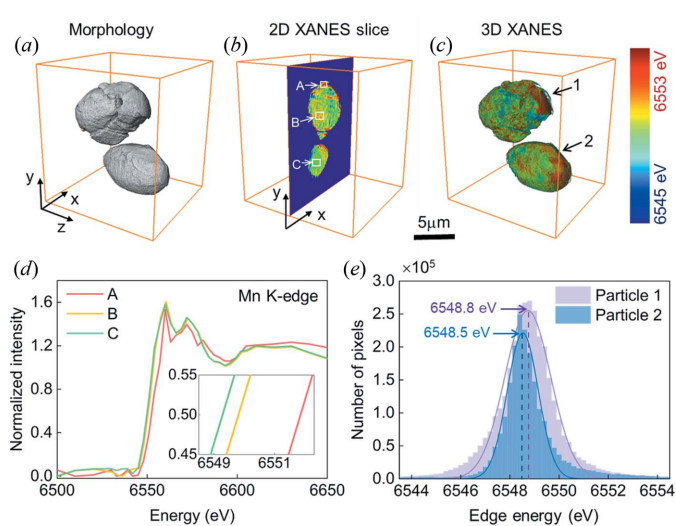
Figure 3
(*a*) and (*b*) 3D visualizations of the squared difference rendering of the original and registered data sets, respectively. (*c*) An MSE plot of raw (red) and aligned (blue) data as a function of the X-ray scan energy.

Figure 4
(*a*) A 3D rendering of the single-energy tomogram of the imaged Li$_x$Ta$_{0.3}$Mn$_{0.4}$O$_2$ cathode particles. Panels (*b*) and (*c*) are the 2D and 3D visualizations of the Mn valence-state distribution, respectively. (*d*) Mn *K* edge X-ray absorption spectra over the regions of interest labeled in panel (*b*). (*e*) The relative probability distribution of the Mn *K*-edge energy over the two particles as labeled in panel (*c*).

energy levels with and without the 3D registration procedure. As shown in Fig. 3(*c*), the 3D registration procedure significantly suppresses the MSE throughout the entire energy window, confirming the effectiveness of our registration approach.

We further conducted a systematic evaluation of this method's performance by purposely inducing motion/deformation on a 3D tomogram and compared the registered 3D image with the known ground truth. To be more specific on the different effects, we separated the translation, rotation, scaling and deformation (see Fig. S1 for an illustration) in several independent tests. To evaluate the method's robustness further, we tested the quality of the registration process with different amounts of salt-and-pepper noise (2%, 5%, 10% and 30%) added to the tomogram (as shown in Fig. S2). By evaluating the MSE between the registered data set and the starting tomogram, the quality of the 3D registration under various conditions can be quantified. The results (as shown in Fig. S3) suggest that the algorithm is rather robust against translation, rotation and scaling errors of the data. The deformation error, however, has a more severe impact on the quality of the 3D registration. When the noise level is low, the implemented algorithm can handle all these motion/deformation errors reasonably well.

With the proposed 3D image-registration procedure, we managed to correct for particle-motion-induced artifacts in the spectro-tomography data. The properly corrected data offer valuable insights into the redox heterogeneity in the two partially delithiated Li$_x$Ta$_{0.3}$Mn$_{0.4}$O$_2$ cathode particles imaged in our experiment. We show the 2D virtual slice and the 3D rendering of the Mn *K*-edge energy over these two particles in Figs. 4(*b*) and 4(*c*), respectively. The spectroscopic fingerprints

of the selected pixels in Fig. 4(*b*) are shown in Fig. 4(*d*). Clear energy offsets are observed in these spectra, indicating different oxidation states of the Mn over the respective localized regions. The surfaces of both particles 1 and 2 [as labeled in Fig. 4(*c*)] are inhomogeneous. To evaluate the overall difference between these two particles, we show in Fig. 4(*e*) their respective probability distributions of the Mn-edge energy over the bulk. Our result not only shows that particle 1 is slightly more oxidized than particle 2, but also reveals a higher degree of redox inhomogeneity in particle 1, as indicated by the broadened peak in Fig. 4(*e*). Particle 1 appears to be in a more delithiated state, which causes particle fracturing and exposes fresh crack surface to the liquid oxidant. These effects collectively modulate the electro-chemo-mechanical behavior of the cathode particle in a deeply charged state.

4. Conclusions

Synchrotron nano-resolution X-ray spectro-tomography is a powerful technique for studying the structural, compositional and chemical complexities in a sample. Successful examples of scientific applications for this technique include energy materials science, industrial catalysis and geoscience. It is, however, a time-consuming method that requires dedicated experimental control. In this work, we have presented a practical case, in which the sample slowly deformed over the course of the spectro-tomographic data acquisition, causing significant degradation of the spectra quality and hindering the data reduction and analysis using the well established workflow. We implemented a 3D tomogram registration method that is robust to the sample deformation. Our result shows clearly improved data quality, which allows us to extract valuable information that is otherwise inaccessible.

Although tremendous efforts have been made to improve the general stability of the experimental configurations on synchrotron beamlines, unanticipated sample deformation can still jeopardize the experimental result. We would point out that the 3D image-registration process is particularly important when conducting imaging at a high spatial resolution. For example, in nano-resolution spectro-tomography, the effective resolution can be as small as 30 nm, which makes it very sensitive to sample motion and/or deformation.

Our development is valuable for handling realistic spectro-tomographic data. Further effort to improve the efficiency is highly desirable.

References

Andrews, J. C., Meirer, F., Liu, Y., Mester, Z. & Pianetta, P. (2011). *Microsc. Res. Tech.* **74**, 671–681.
Brenner, D. J. & Hall, E. J. (2007). *N. Engl. J. Med.* **357**, 2277–2284.
Buffiere, J. Y., Maire, E., Adrien, J., Masse, J. P. & Boller, E. (2010). *Exp. Mech.* **50**, 289–305.
De Chiffre, L., Carmignato, S., Kruth, J. P., Schmitt, R. & Weckenmann, A. (2014). *CIRP Annals*, **63**, 655–677.
Dierolf, M., Menzel, A., Thibault, P., Schneider, P., Kewish, C. M., Wepf, R., Bunk, O. & Pfeiffer, F. (2010). *Nature*, **467**, 436–439.
Eastwood, D. S., Bayley, P. M., Chang, H. J., Taiwo, O. O., Vila-Comamala, J., Brett, D. J., Rau, C., Withers, P. J., Shearing, P. R., Grey, C. P. & Lee, P. D. (2015). *Chem. Commun* **51**, 266–268.
Green, B. (2002). *Canny Edge Detection Tutorial*, http://www.scribd.com/doc/40036113/Canny-Edge-Detection-Tutorial. (Retrieved 6 March 2005).
Hitchcock, A. P. (2015). *J. Electron Spectrosc. Relat. Phenom.* **200**, 49–63.
Kan, W. H., Wei, C., Chen, D., Bo, T., Wang, B. T., Zhang, Y., Tian, Y., Lee, J. S., Liu, Y. & Chen, G. (2019). *Adv. Funct. Mater.* **29**, 1808294.
Kao, T. L., Shi, C. Y., Wang, J., Mao, W. L., Liu, Y. & Yang, W. (2013). *Microsc. Res. Tech.* **76**, 1112–1117.
Liu, Y., Meirer, F., Wang, J., Requena, G., Williams, P., Nelson, J., Mehta, A., Andrews, J. C. & Pianetta, P. (2012). *Anal. Bioanal. Chem.* **404**, 1297–1301.
Liu, Y., Meirer, F., Williams, P. A., Wang, J., Andrews, J. C. & Pianetta, P. (2012). *J. Synchrotron Rad.* **19**, 281–287.
Masci, L., Dubacq, B., Verlaguet, A., Chopin, C., De Andrade, V. & Herviou, C. (2019). *Am. Mineral.* **104**, 403–417.
Meirer, F., Cabana, J., Liu, Y., Mehta, A., Andrews, J. C. & Pianetta, P. (2011). *J. Synchrotron Rad.* **18**, 773–781.
Nelson, G. J., Harris, W. M., Izzo, J. R. Jr, Grew, K. N., Chiu, W. K., Chu, Y. S., Yi, J., Andrews, J. C., Liu, Y. & Pianetta, P. (2011). *Appl. Phys. Lett.* **98**, 173109.
Sakdinawat, A. & Attwood, D. (2010). *Nat. Photon.* **4**, 840–848.
Torikoshi, M., Tsunoo, T., Sasaki, M., Endo, M., Noda, Y., Ohno, Y., Kohno, T., Hyodo, K., Uesugi, K. & Yagi, N. (2003). *Phys. Med. Biol.* **48**, 673–685.
Wang, J., Chen-Wiegart, Y.-C. K., Eng, C., Shen, Q. & Wang, J. (2016). *Nat. Commun.* **7**, 12372.
Wei, C., Xia, S., Huang, H., Mao, Y., Pianetta, P. & Liu, Y. (2018). *Acc. Chem. Res.* **51**, 2484–2492.
Yang, F., Liu, Y., Martha, S. K., Wu, Z., Andrews, J. C., Ice, G. E., Pianetta, P. & Nanda, J. (2014). *Nano Lett.* **14**, 4334–4341.
Yang, Y., Xu, R., Zhang, K., Lee, S. J., Mu, L., Liu, P., Waters, C. K., Spence, S., Xu, Z., Wei, C., Kautz, D. J., Yuan, Q., Dong, Y., Yu, Y., Xiao, X., Lee, H., Pianetta, P., Cloetens, P., Lee, J., Zhao, K., Lin, F. & Liu, Y. (2019). *Adv. Energy Mater.* **9**, 1900674.
Yang, Y., Xu, Z., Steiner, J. D., Liu, Y., Lin, F. & Xiao, X. (2020). *Appl. Phys. Lett.* **116**, 081904.
Yang, Y., Yang, F., Hingerl, F. F., Xiao, X., Liu, Y., Wu, Z., Benson, S. M., Toney, M. F., Andrews, J. C. & Pianetta, P. (2015). *J. Synchrotron Rad.* **22**, 452–457.
Yu, H., Xia, S., Wei, C., Mao, Y., Larsson, D., Xiao, X., Pianetta, P., Yu, Y.-S. & Liu, Y. (2018). *J. Synchrotron Rad.* **25**, 1819–1826.
Yu, Y.-S., Farmand, M., Kim, C., Liu, Y., Grey, C. P., Strobridge, F. C., Tyliszczak, T., Celestre, R., Denes, P., Joseph, J., Krishnan, H., Maia, F. N. R. C., Kilcoyne, A. L. D., Marchesini, S., Leite, T. P. C., Warwick, T., Padmore, H., Cabana, J. & Shapiro, D. A. (2018). *Nat. Commun.* **9**, 921.
Zhang, F., Lou, S., Li, S., Yu, Z., Liu, Q., Dai, A., Cao, C., Toney, M. F., Ge, M., Xiao, X., Lee, W.-K., Yao, Y., Deng, J., Liu, T., Tang, Y., Yin, G., Lu, J., Su, D. & Wang, J. (2020). *Nat. Commun.* **11**, 3050.
Zhu, P., Zhang, K., Wang, Z., Liu, Y., Liu, X., Wu, Z., McDonald, S. A., Marone, F. & Stampanoni, M. (2010). *Proc. Natl Acad. Sci. USA*, **107**, 13576–13581.
Zhu, Z., Yu, D., Shi, Z., Gao, R., Xiao, X., Waluyo, I., Ge, M., Dong, Y., Xue, W., Xu, G. & Lee WK (2020). *Energy Environ. Sci.* **13**, 1865–1878.